RSC Advances

PAPER

View Article Online
View Journal | View Issue

Check for updates

Cite this: *RSC Adv.*, 2022, **12**, 9008

Facile solvothermal synthesis of a MIL-47(V) metal–organic framework for a high-performance Epoxy/MOF coating with improved anticorrosion properties†

Mahmoud Y. Zorainy,[ab] Mohamed Sheashea,[b] Serge Kaliaguine,[c] Mohamed Gobara[b] and Daria. C. Boffito*[a]

Received 9th December 2021
Accepted 15th March 2022

DOI: 10.1039/d1ra08950a

rsc.li/rsc-advances

The vanadium-based metal–organic framework MIL-47 distinguishes itself among other MOFs for its distinctive structure and unique properties (*e.g.*, flexible structure, high thermal stability, and high surface area). The synthesis of MIL-47 has been reported from various metal precursors, including vanadium(III) chloride (VCl_3) as a rich source of metal ions. Attempts have been made to include other starting materials, a step forward towards large-scale production. Synthesis from various solid materials is encouraged, seeking an economic and greener approach. In this study, vanadium pentoxide (V_2O_5), a readily abundant low-cost and thermodynamically stable metal source, was used to synthesize the MIL-47(V) framework *via* a facile solvothermal route. This precursor provides a controllable rate of metal ion production depending on the applied reaction conditions. In our method, the synthesis took place at a low temperature and reaction time (180 °C for 20 h, instead of 220 °C for 72 h), yielding MIL-47 microrods. Moreover, among its unique properties, the metal centers of MIL-47 oxidize under the influence of thermal or chemical treatments, preserving the framework structure. This unusual character is not commonly witnessed in comparable MOF structures. This property can be leveraged in anti-corrosion applications, whereby a redox reaction would sacrifice the framework components, protecting the metal in contact. However, the chemical stability of MIL-47 is doubted against a corrosive medium. Thus, an epoxy coating with 10 wt% MOF loading was incorporated in our investigation to extend the aluminum alloy (AA2024) surface protection for prolonged exposure duration. The uniformity of distribution of the prepared MOF within the epoxy matrix was confirmed using SEM/EDX. Electrochemical impedance spectroscopy (EIS) was used to evaluate the corrosion performance of the coated samples. The results showed that the inclusion of V-MOF offers extended corrosion prevention, over 60 days, for the AA2024 alloy against artificial seawater. The neat epoxy coating could not prevent the corrosion of AA2024 over two weeks of immersion, whereby pitting corrosion was clearly observed. The V-MOF could induce a series of redox reactions leading to the precipitation of vanadium on the cathodic sites of metal surfaces.

Introduction

Metal–organic frameworks (MOFs) have been applied in catalysis,[1] gas adsorption and separation,[2,3] sensing,[4] and drug delivery.[5] MOFs comprise both inorganic and organic moieties, whereby the metal ions or the metal oxo-clusters are connected to polytopic organic linkers resulting in multidimensional frameworks.[6] The synthesis of MOFs has been developing over the last decades targeting alternative, non-conventional approaches for faster reaction times, higher production yields, and controlled morphology.[7] On the other hand, hydrothermal/solvothermal synthesis is still the most commonly used synthesis technique.

Among all MOFs discovered until now, those made out from vanadium are still limited.[8] MIL-47(V) has drawn attention as a result of its large specific surface area ($S_{\text{Langmuir}} = 1320\ \text{m}^2\ \text{g}^{-1}$), high thermal stability in air (400 °C), as well as its derived superior catalytic properties.[8,9] Such a structure is built from infinite $(\text{V–O–V})_n$ chains linked with benzene-1,4-dicarboxylic acid (H_2BDC, also known as terephthalic acid or TPA), yielding a porous 3D orthorhombic structure (Fig. 1).[8] In these chains, each two vanadium atoms share an oxygen atom and

---

[a] Chemical Engineering Department, Polytechnique Montréal, Montréal, QC H3T 1J4, Canada. E-mail: daria-camilla.boffito@polymtl.ca

[b] Chemical Engineering Department, Military Technical College, Cairo, Egypt

[c] Chemical Engineering Department, Laval University, Québec, QC G1V 0A6, Canada

† Electronic supplementary information (ESI) available. See DOI: 10.1039/d1ra08950a

two carboxylic groups of separate linker molecules (Fig. 1a). The formed pores within the structure are rather channels and not cages, whereby each tunnel is bounded by four benzyl units of the H_2BDC linker and four chains of corner-shared VO_6 octahedra (Fig. 1c and d).[8–10]

As synthesized, the MIL-47 framework is isostructural to MIL-53 with its flexible structure and the trivalent metal ions, whereby the bridged oxygen atoms between the metal octahedra belong to terminal hydroxide ligands.[11] However, the metal ions of the MIL-53 structure maintain their valency regardless of the surrounding conditions. The synthesis of MIL-53 has been reported from different transition metals (*e.g.*, Sc, Cr, Fe) of stable (+3) oxidation state.[12–14] In addition, it was successfully obtained from other p-block elements (*e.g.*, Al, Ga, and In).[15–17] On the contrary, MIL-47 was basically built from vanadium, and recent investigations reported the potential incorporation of manganese.[9,18,19]

Upon the synthesis of these MOFs, the as-synthesized structure was found to be soft and dynamic, whereby reversible flexing (breathing) takes place in the presence of external chemical or physical stimuli.[8,9,11] The as-synthesized MIL-47 "MIL-47as" occupies the narrow pores (np) arrangement due to the inclusion of unreacted BDC molecules inside the pores (Fig. 1b). During the thermal activation of the framework in the air, evacuation of the pores takes place and the structure swells, similar to MIL-53 ht, occupying the large pore (lp) arrangement (Fig. 1d). Unlike MIL-53, throughout the activation process, the V^{3+} ions oxidize to V^{4+}, and the μ_2-OH bonds with the metal centers turn into μ_2-O (*i.e.*, vanadyl group (V=O)), but the topology remains unchanged. After calcination, the MIL-53lt keeps its breathing character depending on the transitions between the large-pore (lp) and the closed-pore (cp) arrangements (Fig. 1c and d). In contrast, MIL-47 expresses a relatively rigid structure compared to MIL-53lt, whereby permanent porosity is achieved.[8–11] Hence, the lp → cp transitions were prohibited, and the cp arrangement was not obtainable in the activated form of MIL-47.

In a typical MOF synthesis, different metal salts are incorporated as a source of metal ions, usually soluble ones such as metal chloride, nitrate, or acetate. Recent studies focusing on this approach offered other metal-salt-free choices, for instance, pure metals and alloys, metal oxides, hydroxides, and carbonates.[20] Such solvent-insoluble solids hardly release metal cations in common solvents, and when used as metal precursors, they supply ions at different rates depending on the reaction conditions; hence, controlling the MOF formation rate. Besides, employing these materials offer a greener, more economical, and sustainable route to tune the size and shape of the targeted MOF. For example, Kitagawa *et al.* have adopted these solid materials, especially oxides, as a strategy to obtain MOF templates.[20,21]

When it comes to MIL-47, vanadium(III) chloride (VCl_3) is the most commonly used metal precursor as it is the most reactive.[9,22–28] Nevertheless, VCl_3 is expensive and air-sensitive. It is unstable and easily decomposes when it comes in contact with the ambient atmosphere; thus, extra caution has to be paid while handling this material. As a result, weighing usually takes place in a nitrogen-filled glove box, which is inconvenient when scaling up the process. Recent investigations have also involved the use of ammonium metavanadate (NH_4VO_3) as a less expensive, more stable, and readily available vanadium precursor.[29] On the other hand, upon thermal decomposition of MIL-47, a mixture of vanadium(IV) and vanadium(V) oxides (VO_2 & V_2O_5) is left as a residue after the decomposition of the organic linker. *Vice versa*, vanadium dioxide (VO_2) was successfully employed in the synthesis of MIL-47.[30,31] However,

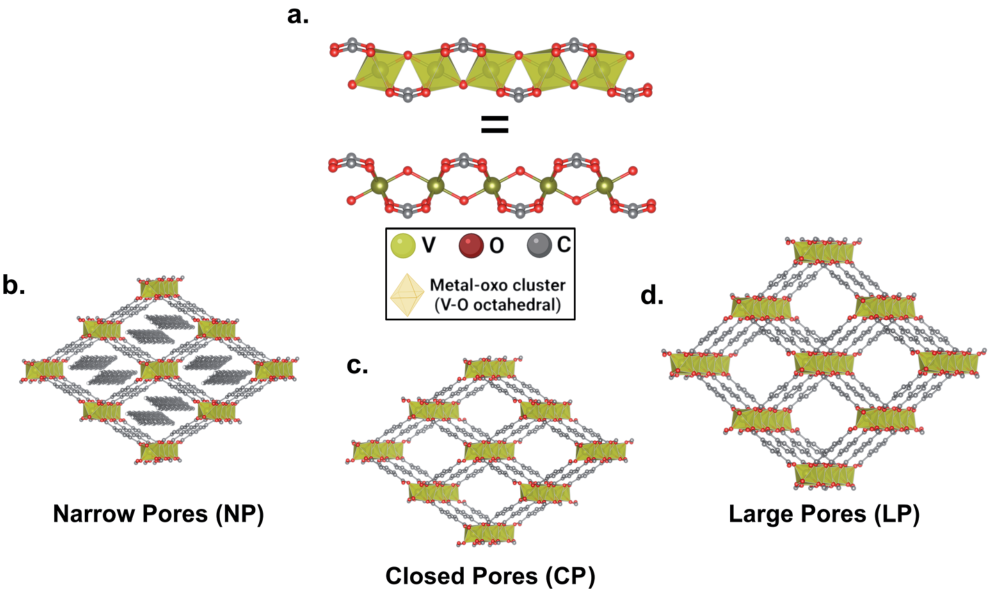

Fig. 1 The structure of the vanadium MOF, MIL-47, expressing its flexibility under the effect of external stimuli. (a) Infinite (V–O–V) one-dimensional chains. (b) Narrow pores. (c) Closed pores. (d) Large pores. Color code: yellow-vanadium, red-oxygen, grey-carbon, hydrogen atoms were omitted for clarity.

to our best knowledge, V_2O_5 has not been reported as a precursor to MIL-47 yet, but only in the synthesis of another framework isomer using the 1,4-naphthalenedicarboxylic acid linker (*i.e.*, $[V(OH)ndc]_n$ MOF).[32]

Metal corrosion is a major problem in the industrial and manufacturing fields. Its spontaneous nature resulting from the surrounding interactions with the metal surface leads to a significant loss in the metal physicochemical properties.[33] Aluminum alloy (AA2024) is extensively applied in the aircraft industry because of its high strength-to-weight ratio, high fatigue resistance, and toughness.[34] However, this alloy does not stand against corrosion in atmospheric conditions. Consequently, cladding or coating along with an inhibitor is usually applied. Organic coatings, such as epoxy, are an effective, practical, and cost-effective approach that can be applied to protect most metal substrates.[35] In order to achieve a prolonged protection lifetime, researchers have applied various strategies in which the incorporation of nanoporous materials, like carbon nanotube, graphene oxide, and nano-silica, comes on top. Recently, research considering reinforcing epoxy with MOFs and achieving advanced organic coatings of multi-functions is highly expanding.[36–38] Moreover, functionalization of MOFs for bonding with the nanofillers and the barrier coating has also been researched for a more advanced coating, providing a long-term protection for the metal-surface.[39–45]

Generally, metal corrosion is inhibited, reduced, or controlled by either adsorption-blocking or electrochemical actions.[46] An inhibitor prevents a metal or an electrolyte from coming into contact with the other side of a porous substrate. This barrier is formed by a combination of physisorption and chemisorption. Inhibitors usually interact through the adsorption mechanism by forming a protective film or layer by physisorption at the metal/electrolyte interface. They can also interact chemically to form an insoluble complex barrier hindering the direct contact between the metal surface and the corrosive electrolyte.[46] For MOFs, recent studies reported that the inhibition follows the adsorption-blocking mechanism:[42–44] indeed, in MOFs, the organic linker confers different functional groups that are electron donor heteroatoms with π bonds.[46] Corrosion inhibition by coordination polymers or MOFs through electrochemical action is less common. Studies considering the anti-corrosion properties of MOFs are still scarce.

The presence of organic linkers within the structure of MOFs makes them compatible with the polymeric matrices.[36] Also, they can be functionalized to increase their interaction for more advanced MOFs/polymer nanocomposites. Moreover, the metal centers can accelerate the cross-linking of these networks as active Lewis-acid sites, catalyzing the epoxy ring-opening reaction. For example, MIL-101(Cr), with its high surface area and highly active metal centers, facilitates the curing of thermoset polymers used as organic corrosion barriers. Such a porous structure significantly increases the amount of heat released during curing even at very low loadings.[47] Our group has previously studied the anti-corrosion performance of a cerium(III)/melamine coordination polymer and the mechanism behind the interactions taking place.[48,49]

Here, we studied the solvothermal synthesis of the MIL-47 framework from V_2O_5 as an inexpensive, widely available, and thermodynamically stable precursor, a step forward towards scaling up the production of this MOF. In similar syntheses from oxides, one of the main drawbacks is the inclusion of unreacted metal oxide among the product as a contaminant, which we could avoid with the method proposed. The narrow-pore MIL-47(V^{III})as was fully characterized before its incorporation in the epoxy coatings for the anti-corrosion experiments. Moreover, the performance of the MOF/epoxy coating was evaluated, compared to neat epoxy coating, as an improved corrosion barrier to aluminum alloy AA2024 in a chloride-rich environment.

Results and discussion

MIL-47 characterization

The recorded PXRD diffractogram was very similar to the simulated pattern of as-synthesized MIL-53 and MIL-47 (Fig. 2). The pattern showed recognizable high-intensity peaks in the 5°–30° 2θ-range, with the major diffraction peaks at around $2\theta = 8.8°, 10.1°, 14.8°, 17.7°, 24.1°$, and $26.7°$.[9,50] Moreover, in comparison with the pattern of the original vanadium precursor, the main diffractions of V_2O_5 at $2\theta = 15.4°, 20.3°, 21.7°$, and $26.2°$ were not detected in the recorded pattern, indicating a pure MOF product without any residual oxide.[51] Hence, the adopted synthesis technique (solvothermal method) was able to induce the release of the required metal cations from V_2O_5 as a precursor under the selected reaction conditions. The simple washing procedure applied was sufficient to remove unreacted precursors. On the other hand, upon thermal activation of the MIL-47 framework, the structure occupies the less flexible large-pore form. The XRD pattern for the activated

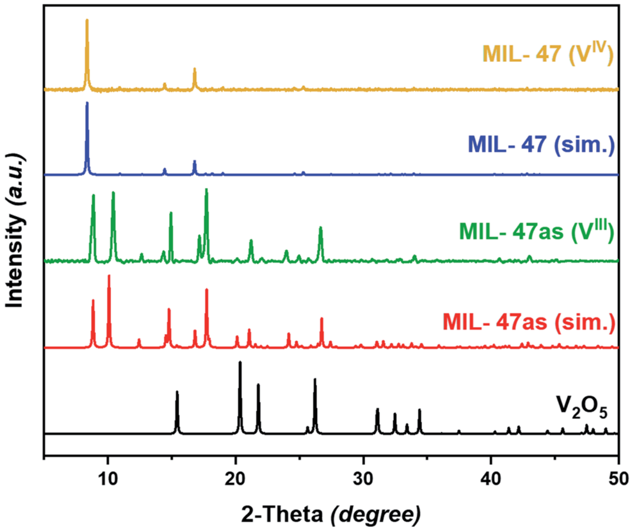

Fig. 2 The XRD patterns for the MIL-47(V) metal–organic framework compared to simulations. V_2O_5 – "black"; MIL-47as (simulation) – "red"; MIL-47as(V^{III}) – "green"; MIL-47 (simulation) – "blue"; MIL-47(V^{IV}) – "yellow"; (calculated patterns reproduced *via* Mercury/CSD simulated files: "IDIWIB" and "IDIWOH," respectively).

MOF form was identical to the simulation of the reported MIL-47, whereby the prominent diffraction peaks were recognizable in the 5°–20° 2*θ*-range, specifically at 8.3°, 14.4°, and 16.8° (Fig. 2).[9] Once again, no diffractions of the metal oxide occurred in the activated MOF pattern.

Fourier-transform infrared spectroscopy (FTIR) was employed to confirm the formation of the targeted MOF and the linkage between the vanadium cations and the organic ditopic H_2BDC ligands. The vibrational spectrum of the obtained crystals agreed well with that reported for the MIL-47 framework (Fig. S2†). In order to ensure that the synthesized MOF is metal-oxide free, Raman spectroscopy was used as a selective technique to investigate such possible inclusion of other materials within the MOF crystals (Fig. S3†). It clearly showed that despite being prepared from a metal oxide precursor, the synthesis technique reported here produced pure MOF crystals without any oxide residue.

The thermogravimetric analysis (TGA) technique was utilized to investigate the thermal stability of the MOF product. This technique can also indicate the inclusion of metal oxide residue based on the increase in the final weight percentage. Heating the MIL-47as sample from room temperature to 800 °C resulted in three weight-loss steps (Fig. 3). The first step corresponds to the evaporation of residual solvents, whereby a gradual weight loss (equivalent to 5–7%) occurs at temperatures ≤200 °C. The second step of almost 30% weight-loss is in the region between 200–350 °C, originating from the oxidation of the V^{3+} metal centers and the loss of the hydroxide groups bonded to the vanadium oxo-chains. At these temperatures, the thermal activation of the MOF occurs, whereby heat removes the unreacted H_2BDC linker from the framework's pores. Finally, the detachment of the organic linker and decomposition of the framework structure takes place in the third step between 375–425 °C, showing a weight loss of 40% with a mixture of VO_2 and V_2O_5 remaining as residue after the experiment.[9,22]

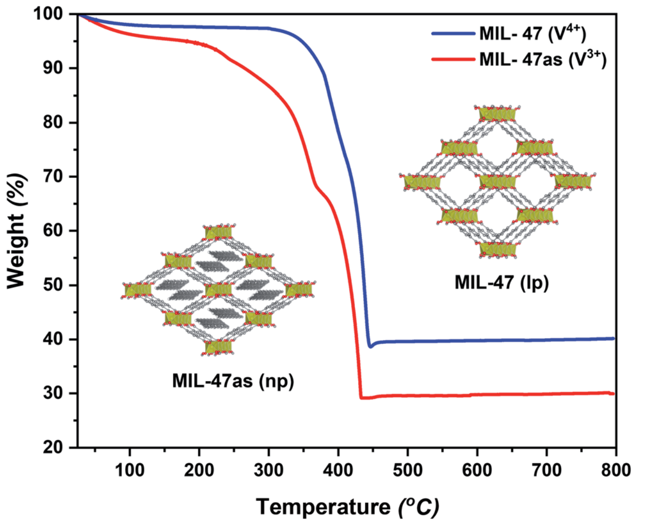

Fig. 3 TGA curves of the as-synthesized MIL-47 "MIL-47as" powder compared to the thermally activated sample (MIL-47), showing the different weight loss steps and the transformation from the np to the lp forms of the structure.

Overall, the MIL-47as sample lost *ca.* 70% of its initial weight, comparable to published TGA data.[8,9,22,23,25,28,29,52] Hence, confirming the purity of the obtained MOF and the absence of any residuals from the metal precursor. However, the separation and washing steps significantly affect the quality of the MOF product. Excessive washing can lead to partial decomposition as a result of its low chemical stability.[52] The TGA results confirmed that the above-reported washing procedures were convenient to achieve a pure product without decomposition.

On the other hand, the thermally activated sample (MIL-47) showed a single dominant weight-loss step (Fig. 3) aside from the initial weight loss of 2–3% below 100 °C resulting from the evaporation of the adsorbed water.[15] After this slight weight loss, a plateau follows, skipping the metal centers' oxidation and the pore evacuation step until the decomposition of the framework between 350–450 °C, expressing a large-pore (lp) arrangement.[9] Once again, the TGA curve of this sample agreed with the previous studies, whereby a total weight loss of *ca.* 60% was witnessed (10% less than MIL-47as) as a result of the framework activation and oxidation.[9]

The SEM images of the MOF samples confirmed the results reported above. Owing to the considerable difference in density between the as-synthesized crystals of MIL-47(V) framework and the V_2O_5 particles, SEM operated on the back-scattered electron mode (detector) was selected to screen the sample, whereby no traces of any foreign particles were found among the MOF crystals. On the other hand, the morphology of the crystals was studied using the secondary electron detector (Fig. 4). The images showed the rod-like shape of the obtained crystals with a length of a few microns (<10 μm, Fig. 4a and b). Furthermore, the images of the thermally activated samples showed typical crystals with no change in the morphology compared to the as-synthesized sample (Fig. 4c).

The EDX elemental analysis and mapping of the as-synthesized sample confirm the main composition of the MOF structure, whereby the three main elements V, O, and C were detected. These three elements were homogeneously distributed all over the sample (Fig. 5). Also, the measured concentration of each element agreed with the reported formula of the MIL-47 MOF, whereby the abundance of each element was found as (at%): C 49%, O 37%, and V 14%.[9]

Corrosion performance

Before testing the corrosion resistance of the prepared coatings, the adhesion and the thickness of both the neat epoxy and the MOF/epoxy coatings were investigated. The results of the crosshatch adhesion test, applied to evaluate the adhesion of both types of coating, revealed an excellent adhesion of the coating to the surface of the substrate (Fig. S4†). Next, using SEM/EDX microscopy, the thickness of each coating was investigated. The cross-section images showed uniform coating with a constant thickness of around ≈10 ± 2 μm (Fig. 6).

Also, the surfaces of the coatings were free from cracks and contained no voids in between layers. Both coatings displayed

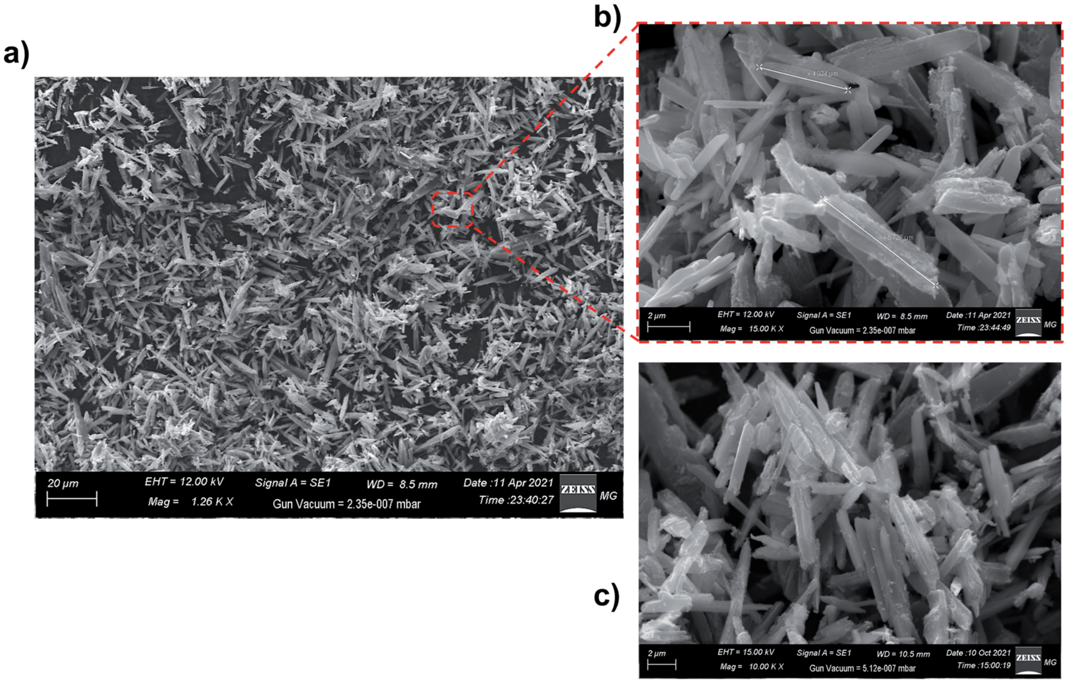

Fig. 4 The SEM images of the MIL-47 samples at different magnifications. (a) and (b) as-synthesized MIL-47, (c) thermally activated MIL-47.

excellent adhesion to the AA2024 substrate, whereby there is no sharp edge between the coating and the metal substrate (*C* represents the epoxy matrix in both samples). Furthermore, the cross-section image of the MOF/epoxy coated sample depicts a uniform distribution of the vanadium-MOF within the epoxy matrix; however, the epoxy-coated AA2024 sample did not show any vanadium. Due to the low thickness of the MOF/epoxy layer, it can be used as a pre-treatment layer applied before applying the subsequent paint topcoats.

Moreover, the homogeneity of the MOF/epoxy coating was thoroughly investigated. The uniform distribution of the MIL-47as crystals within the epoxy matrix was monitored and validated using SEM/EDX (Fig. 7a). The SEM images of the coating surface obtained from the back-scattered detector showed that the V-MOF crystals were fully integrated into the organic matrix, preserving the same particle size presented in Fig. 4 and 5. Based on the density difference between the MIL-47as micro-rods and the hardened epoxy matrix, the MOF crystals appear as white particles randomly dispersed over the darker grey/black colored epoxy coating (Fig. 7a). Furthermore, the elemental spot analysis of the coating confirmed the homogenous distribution of vanadium all over the organic epoxy matrix in

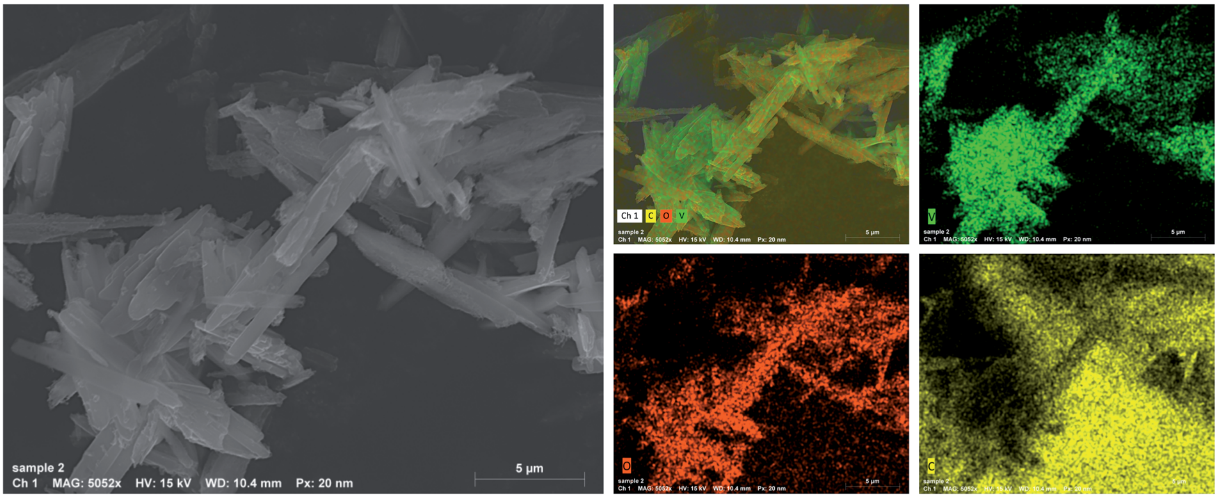

Fig. 5 Elemental mapping of the as-synthesized MIL-47 sample obtained through the solvothermal technique, expressing the homogenous distribution of the elements over the whole MOF crystals. Color mapping: V – bright green, O – orange, C – yellow.

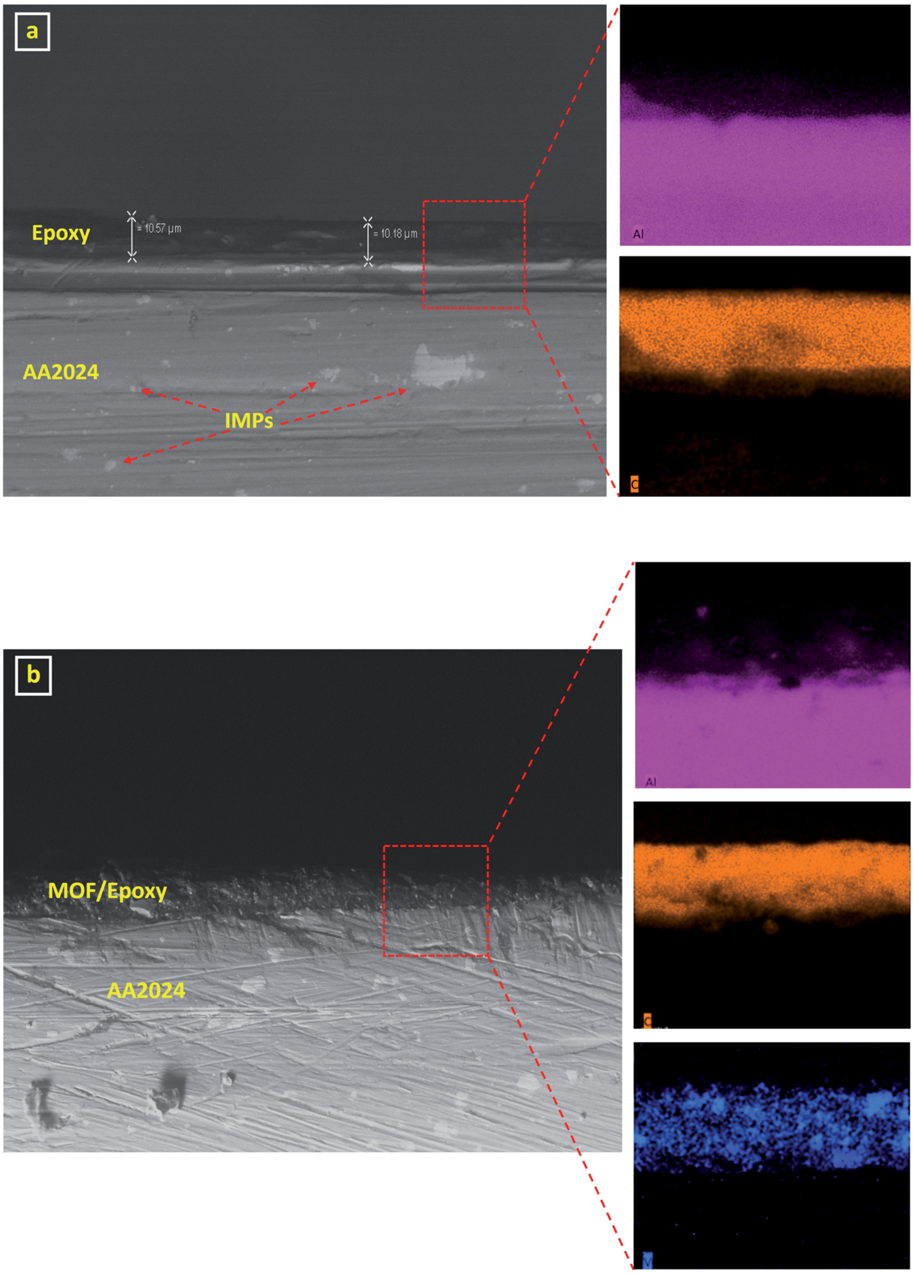

Fig. 6 Side view for the cross-section of (a) neat epoxy (b) MOF/epoxy coated AA2024 samples under the SEM with their elemental EDX mapping. Color mapping: Al – purple, C – orange, V – blue.

agreement with the previous results. However, nitrogen and aluminum were also detected in addition to the main MOF elements reported above (Fig. 7b). Nitrogen results from the DETA hardener as a tertiary amine responsible for the epoxy ring-opening and the initiation of the polymerization process, while the noticeable aluminum peak belongs to the substrate as a result of the small coating thickness employed in this case.

The corrosion prevention behavior of the coated samples was assessed *via* electrochemical impedance spectroscopy (EIS). Such a technique offers computable data reflecting both the corrosion and coating degradation processes throughout the whole course of immersion in the corrosive environment. Starting with the neat epoxy-coated AA2024 sample, the trend is linear with a slope approaching −1, expressing a general capacitive behavior at high and mid-range frequencies (Fig. 8a) that maintained over the 3 weeks immersion period in the corrosive electrolyte, 3.5% wt NaCl.[53] This epoxy coating acts as a barrier showing an initial high impedance of 6 MOhm cm^2 at 0.01 Hz after 3 days of immersion, whereby the corrosive solution would not effectively diffuse into the coating/surface interface during this early stage. However, the impedance gradually decreases through the end of the immersion test, losing more than an order of magnitude of impedance to about 0.3 MOhm cm^2 after 21 days of immersion.

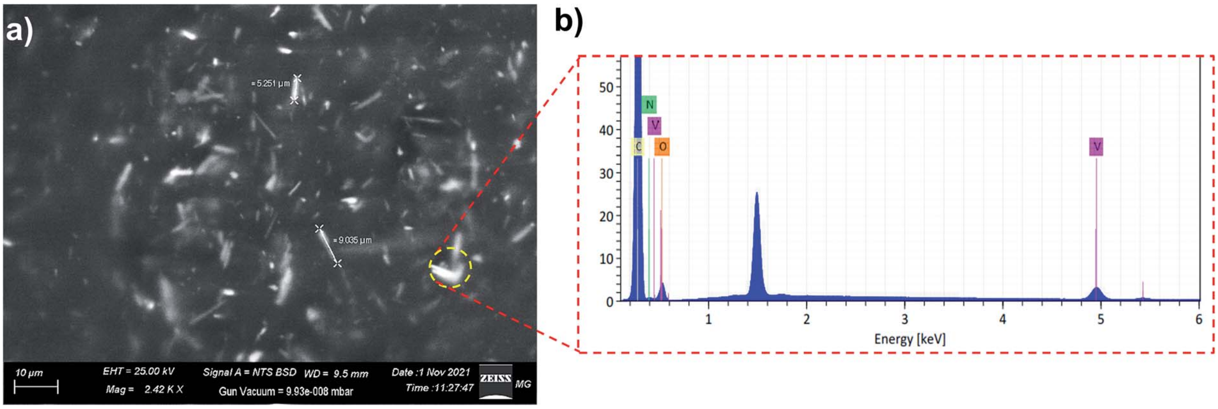

Fig. 7 (a) SEM image of the MOF/epoxy coating surface (top view) (b) EDX spot analysis of the selected area, with the peak between 1–2 keV belonging to the aluminum substrate. Color code: V – pink, C – yellow, N – light green, O – orange.

In addition, the total impedance (|Z| at 0.01 Hz) showed a continuous decrease throughout the immersion test with the rise of a new time constant at the low-frequency range after 14 days of immersion. This time constant slightly increases afterward, as indicated by the phase angle plot (Fig. 8b). The figure clearly shows that the coating sustained the high phase angle at the high-frequency range during the immersion time. Nevertheless, the decrease in the impedance at the low-frequency range along with the existence of this new time constant indicate the degradation of the organic epoxy coating and the deterioration of its properties as a barrier. This time constant is usually attributed to the relaxation of the mass transport process due to the formation of the corrosion products.[54] This activity is accompanied by pitting corrosion in different spots, observed after 14 days of immersion, which clearly confirms the breakdown of the epoxy coating. This behavior takes place in similar physical, non-active barrier coating systems.

The pitting corrosion formed in the neat epoxy-coated sample was investigated by the EDX elemental mapping (Fig. S5†). According to the mapping, aluminum, carbon, copper, magnesium, and oxygen were all detected. All the detected metals represent the different components of the aluminum alloy, while carbon mainly belongs to the epoxy coating. Over the scanned area, several spots were found to be of a different nature (red circles in Fig. S5†). Closer inspection of these spots revealed a recognizable decrease in the carbon content and a corresponding increase in the other metals in the same area, indicating the degradation of the coating around these pitting centers. Also, the images clearly show the presence of several cracks within the coating matrix.

The corrosion process starts when the electrolyte diffuses through the coating to the inner metallic surface. Aluminum/copper alloys, AA2*xxx*, are subjected to pitting corrosion in an aerated chloride-containing environment due to surface inhomogeneities. The intermetallic particles containing copper and magnesium (such as $AlCu_2$, AlCuMnFe, and Al_2CuMg) have a higher potential to corrode than the aluminum matrix.[55] In aerated NaCl solution, these intermetallic particles act as a cathode with respect to the matrix, at which the cathodic reaction (reduction of oxygen) takes place on the surface of these intermetallic particles. Consequently, the most affected areas are those adjacent to these intermetallic particles.[56,57] In addition, the surface of AA2024 alloy contains up to 3% of intermetallic particles. Although these particles enhance the

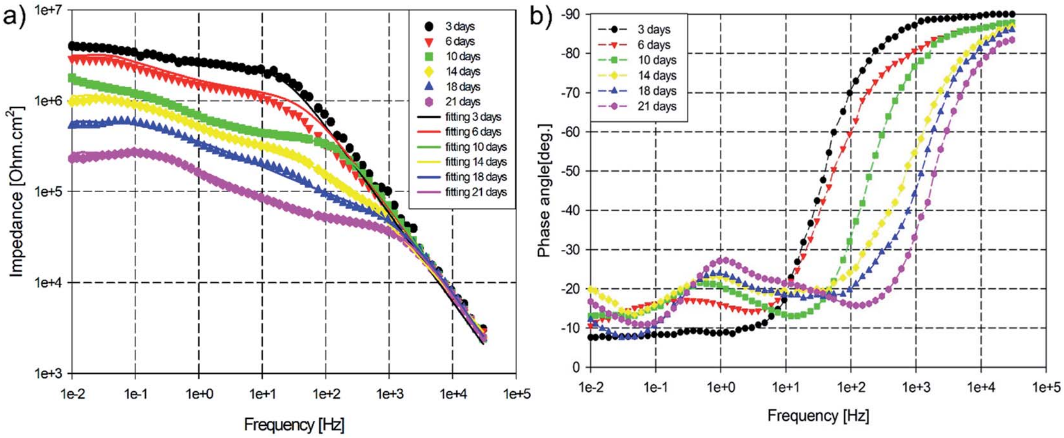

Fig. 8 Bode plots of the epoxy coated AA2024 samples in 3.5% NaCl solution at room temperature. (a) Impedance, (b) phase angle.

mechanical properties (mainly the strength) of the alloy, they would increase its susceptibility to localized corrosion resistance (mainly pitting corrosion).[58–61]

Unlike the neat epoxy coating, the corrosion performance of the MOF/epoxy coating expressed a different behavior (Fig. 9a). The impedance clearly showed a slight decrease in the early stage of immersion (around 2 MOhm cm^2 at 0.01 Hz after 3 days of immersion) compared to that of the neat epoxy sample. In addition, this coat did not display the capacitive behavior measured in the high and mid-range of frequencies for the neat epoxy coating. This behavior change can be attributed to the variation in the hydrophilic character of epoxy as a result of the MOF crystals and their highly porous nature.[62] The impedance curve also shows a continuous decrease in the measured values during the first three weeks of immersion (similar to the neat epoxy coating). However, the impedance seems to be stable after that period, showing no sign of corrosion or delamination over the rest of the 60 days immersion course. During this period, and despite the slight decrease in the impedance at high and mid-range frequency, the total impedance ($|Z|$ at 0.01 Hz) remained stable. This maintained impedance stability without the observation of any new time constant indicated the stability of the coating/metal interface, proving the ability of the MOF/epoxy coating to prevent AA2024 oxidation in 3.5% NaCl solution.

The phase angle plot of the MOF/Epoxy coating (Fig. 9b) showed a sharp reduction in phase angle values at the high-frequency range (3×10^5 Hz) during the first three weeks of immersion. After this period, the coating becomes stable for the rest of the 60 days. The curve also reveals two time constants around 10^4 and 6 Hz corresponding to the coating/electrolyte and coating/metal interfaces, respectively. In addition, the latter time constant gradually shifts from 6 Hz to 0.4 Hz, while the maximum of this time constant peak seems to be stable during the immersion test. Such behavior suggests the formation of an interfacial layer that can protect the metal from corrosion.[57] The test was terminated once the delamination of the coating began to appear after 65 days (Fig. S6†). Although the coating was delaminating (red circles in Fig. S6†), the sample's surface did not show any evident corrosion after 65 days of immersion in 3.5% wt NaCl solution.

The Nyquist plots of the epoxy coated AA2024 sample (Fig. 10a) in the corrosive 3.5% NaCl solution clearly showed two time constants that characterize a typical physical barrier coating. Both the capacitance and resistance components of the impedance continue to decrease with the immersion time, as indicated by the shrinkage of the time constant radii. This decrease in the corrosion impedance was accompanied by the observation of pitting corrosion, indicating the failure of the coating. Contrarily, the Nyquist plots of the MOF/epoxy coated AA2024 sample (Fig. 10b) revealed two impeded semicircles covering both high- and low-frequency ranges. The semicircles at the low-frequency range clearly display irregularity due to the inhomogeneity of the metal surface and/or the frequency dispersion.[63] The plots feature the presence of a capacitive loop at the low-frequency range with a radius decreasing with the immersion time during the first 10 days. The most noticeable observation from this figure is that after the initial period of immersion, 10 days, the diameter of the capacitive loop at the low-frequency range seems to be stable over the rest of the immersion period. This stability at low frequencies is related to the corrosion resistance of the metal substrate.[64] This behavior indicates that the MOF/epoxy coating can provide corrosion protection for AA2024 in the 3.5% NaCl solution over an extended period of time. Such an event agrees and confirms the optical observations, whereby the coating does not show any sign of delamination or blistering.

The change in hydrophobicity of these coatings plays a significant role in their corrosion protection performance and influences the behavior of these samples. Hence, the contact angle of both neat and MOF/epoxy coatings was measured at the beginning of immersion (test) using distilled water. Contact angles of 86° and 53° (Fig. S7†) were measured for the neat epoxy and the MOF/epoxy samples, respectively, suggesting a considerable change in the impedance behavior of both coatings in the high-frequency range being related to the increase in hydrophilicity of the coating.

For a better understanding of the corrosion behavior of the coated samples, the EIS data for both epoxy coating systems

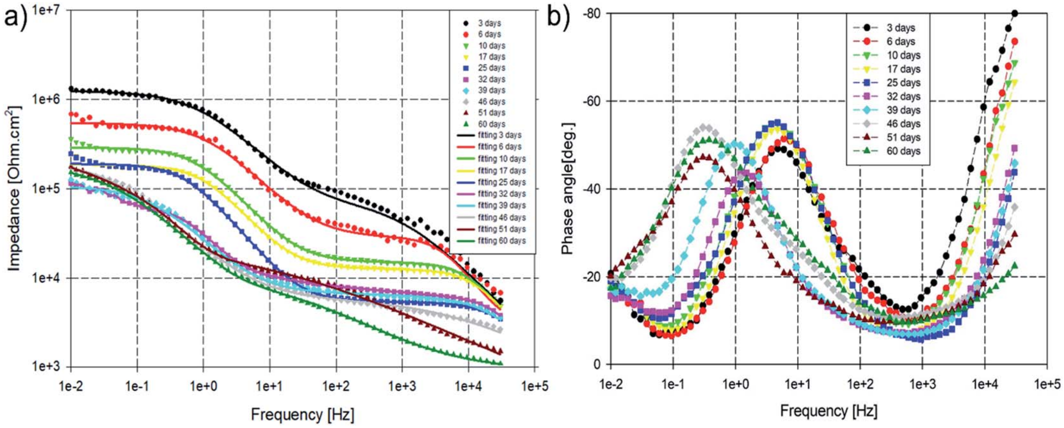

Fig. 9 Bode plots of the MOF/epoxy coated AA2024 samples in 3.5% NaCl solution at room temperature. (a) Impedance, (b) phase angle.

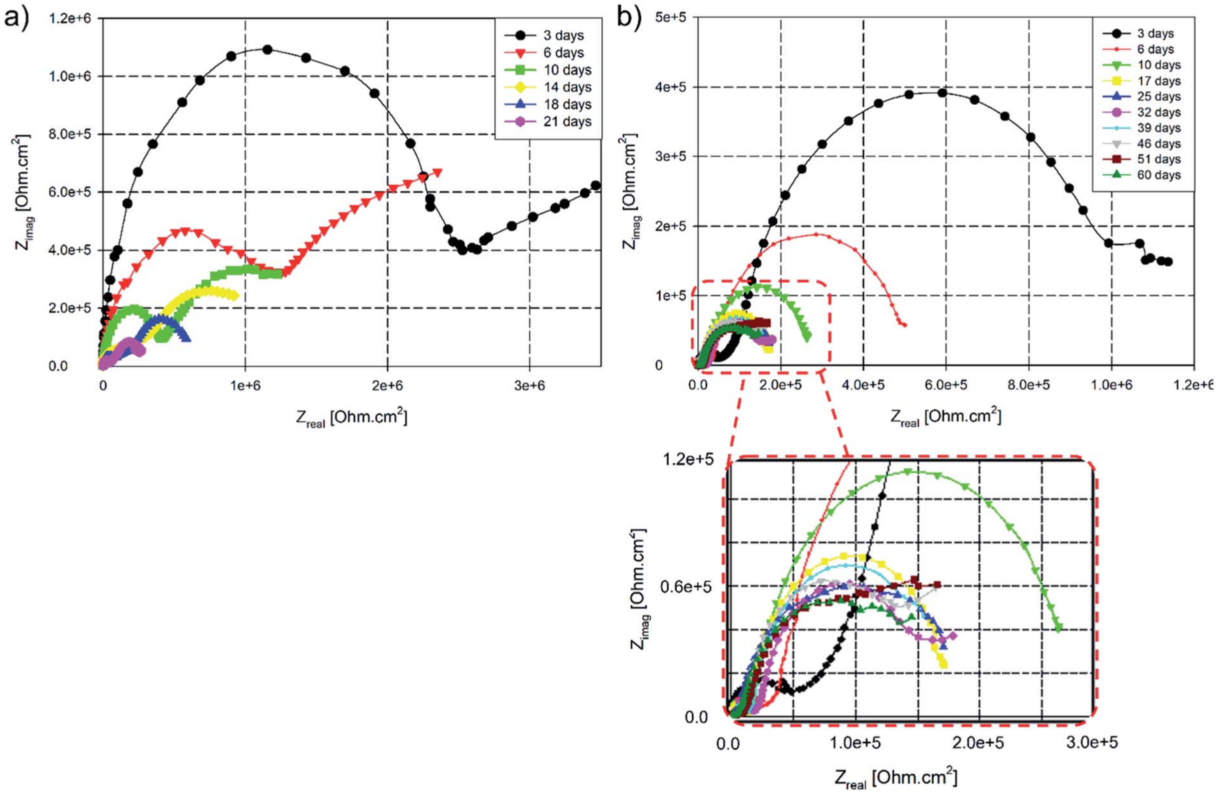

Fig. 10 Temporal Nyquist plots for the coated AA2024 samples in 3.5% NaCl solution at room temperature (a) neat epoxy, (b) MOF/epoxy coating.

were fitted to equivalent circuits, as presented in Fig. 11. Fig. 11a represents the equivalent circuit of the neat epoxy during the first week of immersion. This figure consists of electrolyte resistance (R_s), coating capacitance (C_{coat}), and coating pore resistance (R_{coat}). In comparison, Fig. 11b shows a typical equivalent circuit of an organic coating, representing both the neat epoxy after a week of immersion and the MOF/epoxy coating during the entire immersion course. In Fig. 11b, two-time constants were observed during immersion in the corrosive solution for both epoxy coatings. The first time constant at high frequencies is assigned to the capacitance (C_{coat}) and pore resistance (R_{coat}) of the coating, while the other in the low-frequency range one represents the double-layer capacitance (C_{dl}) and the charge transfer resistance (R_{ct}) of the corrosion areas. In these circuits, constant phase element (CPE) was used as a replacement for pure capacitance to attain more accurate results from experimental data fitting due to the non-ideal behavior of pure capacitors.[65] The capacitance can be calculated from CPE parameters according to the following equation,[66] and the electrochemical parameters are reported in Tables 1 and 2.

$$C_{dl} = \frac{Y_o \cdot \omega^{(n-1)}}{\sin\left(\frac{n\pi}{2}\right)} \tag{1}$$

where Y_o is the CPE constant, ω is the angular frequency (rad s^{-1}), and n is the CPE exponent where $n = 1$ for an ideal capacitor. The EIS fitting quality is accepted when the goodness of fitting is less than 1×10^{-3}.

Fig. 12 shows the coating capacitance and resistance changes over the immersion time for the neat epoxy coated

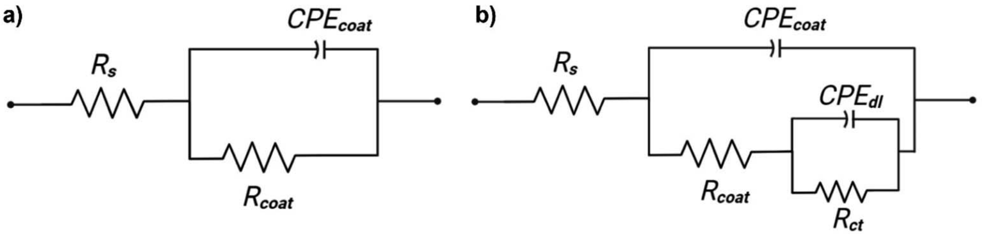

Fig. 11 The equivalent circuits applied in the fitting of the impedance data for (a) neat epoxy until 3 days of immersion, (b) neat epoxy after 3 days and MOF/epoxy.

Table 1 The electrochemical parameters extracted from the fitting of the EIS results of the neat epoxy sample after immersion in a corrosive 3.5% NaCl solution at various immersion times

Sample	Time [day]	R_s [Ω cm^2]	Q_{coat} [10^{-9} F cm^2 s^{n-1}]	n_1	R_{coat} [10^4 Ω cm^2]	Q_{dl} [10^{-7} F cm^2 s^{n-1}]	n_2	R_{ct} [10^5 Ω cm^2]
Epoxy	3	3.2	2.91	1.00	61.24	—	—	—
	6	4.9	2.59	0.95	49.31	5.49	0.97	34.12
	10	2.3	1.98	0.92	45.54	9.26	0.94	29.81
	14	1.8	2.65	0.88	29.18	10.9	0.93	9.21
	18	1.3	5.29	0.87	5.31	14.71	0.87	7.51
	21	1.3	27.18	0.76	2.70	69.16	0.79	4.22

AA2024 sample. Fig. 12a shows a slight decrease in R_{coat} during the course of immersion in the corrosive electrolyte, while the values of the C_{coat} show a kind of stability during the first two weeks of immersion followed by an increase in its value. This behavior reflects the hydrophobic properties of the epoxy coating. The R_{ct} of the epoxy coated AA2024 sample continuously decreases during the immersion period, as depicted in Fig. 12b, in which C_{dl} gradually increases with immersion time. The behavior is attributed to the diffusion of the corrosive electrolyte to reach the coating/metal interface followed by the interaction with the metal surface forming corrosion products. These results specify the rapid degradation of the neat epoxy coated AA2024 in this Cl$^-$-containing solution forming pitting corrosion.

Fig. 13a and b show the experimental EIS data fitting results related to the MOF/epoxy coating on the equivalent circuit. Both figures have the same trend of changing parameters; the C_{dl} and C_{coat} increase at the beginning of immersion then seem to be steady while R_{ct} and R_{coat} decrease at the beginning then seem to have plateau values. In contrast to the continuous change in the coating/metal interface' parameters (R_{ct} decreases and C_{dl} increases) of epoxy coating with the observation of pitting corrosion, the MOF/epoxy coating shows higher stability of these interface parameters after 4 weeks of immersion. The stability of the coating/metal interface resistance and capacitance indicates a considerable enhancement of the resistance to the corrosive electrolyte diffusion, which can be attributed to the presence of the MIL-47as crystals within the epoxy coating.[53] This behavior is usually presented upon the development of a protective layer formed as a result of the presence of the V-MOF within the epoxy matrix.

Mechanism of interaction

AA2024 is an aluminum alloy with a high mechanical strength owing to the intermetallic particles (IMPs). These IMPs decrease the corrosion resistance of the alloy by altering the corrosion potential of the alloy's surface.[58,59] Such an alloy is usually susceptible to localized corrosion, mostly pitting, in an aerated Cl$^-$-containing solution, and the degree of pitting depends on the nature of these IMPs.[55] Generally, under free corrosion conditions, IMPs of AA2024 (such as the S-phase) are active species compared to the Al matrix due to the presence of magnesium. Magnesium will then dissolve, leaving copper behind, which acts as a local cathode assisting oxygen reduction reaction. In this aerated solution, the main reduction reaction would be that of oxygen reduction resulting in the creation of some intermediates as follows:

$$\tfrac{1}{2}O_2 + H_2O + 2e^- \rightarrow 2OH^- \tag{2}$$

$$O_2 + H_2O + 2e^- \rightarrow H_2O_2 + OH^- \tag{3}$$

The oxygen reduction occurs on the cathodic areas in which IMPs exist, representing almost 3% of the total alloy surface area.[49] The oxidation reaction takes place by the dissolution of the Al matrix existing around these IMPs, developing pitting. The Al matrix dissolution (oxidation reaction) undergoes a series of reactions that finally forms the Al(OH)Cl$^+$ complex, which is easily dissolved in the aqueous solution.[49]

$$Al + 3H_2O \rightarrow Al(OH)_3 + 3H^+ + 3e^- \tag{4}$$

$$Al + 2H_2O \rightarrow AlO(OH) + 3H^+ + 3e^- \tag{5}$$

Table 2 The electrochemical parameters extracted from the fitting of the EIS results of MOF/epoxy sample after immersion in a corrosive 3.5% NaCl solution at various immersion times

Sample	Time [day]	R_s [Ω cm^2]	Q_{coat} [10^{-7} F cm^2 s^{n-1}]	n_1	R_{coat} [10^4 Ω cm^2]	Q_{dl} [10^{-9} F cm^2 s^{n-1}]	n_2	R_{ct} [10^5 Ω cm^2]
MOF/epoxy	3	3.2	2.08	0.75	7.12	0.94	0.74	11.81
	6	4.9	3.92	0.79	2.60	1.62	1.00	5.22
	10	2.3	8.78	0.85	1.48	1.86	0.95	2.74
	17	1.8	11.25	0.88	1.25	2.07	0.93	1.74
	25	1.3	18.03	0.89	0.54	4.01	0.88	1.85
	32	1.3	77.16	0.76	0.64	69.38	0.79	1.66
	39	2.4	89.15	0.77	0.65	91.72	0.76	1.21
	46	3.1	90.48	0.72	0.61	48.41	0.45	2.08
	51	1.8	63.28	0.97	1.24	44.51	0.36	2.97
	60	2.1	79.92	0.85	1.03	69.92	0.52	1.91

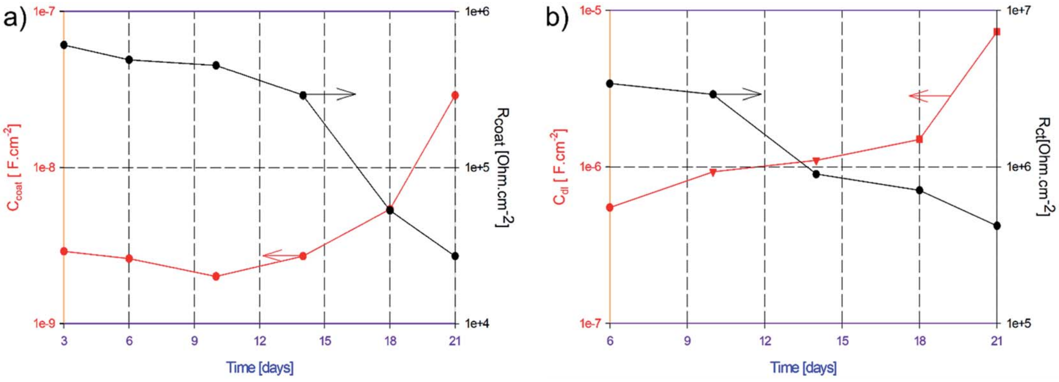

Fig. 12 The change in (a) C_{coat} and R_{coat} and (b) C_{dl} and R_{ct} values regarding the epoxy coated AA2024 sample in 3.5% NaCl solution *versus* the immersion time.

$$Al + 3/2H_2O \rightarrow Al_2O_3 + 3H^+ + 3e^- \quad (6)$$

$$Al(OH)^{2+} + Cl^- \rightarrow Al(OH)Cl^+ + 3H^+ + 3e^- \quad (7)$$

In the previous section, the results clearly showed that the presence of the V-MOF (MIL-47as) particles within the epoxy matrix significantly reduced the corrosion rate of AA2024 in an aerated NaCl solution. Generally, the vanadate treatment can reduce the oxygen reduction reactions similar to that of chromate. This interaction with the AA2024 alloy can be attributed to the reduction in the galvanic current of the metal surface, in which the vanadate species selectively cover the cathodic sites (*i.e.*, precipitating on the IMPs forming a stable film).[67] The rate-determining step of this film formation is the diffusion of vanadate species from the bulk to the IMPs.[68] In this context, the presence of a vanadate layer over the IMPs hinders the oxygen adsorption on the surface, effectively reducing corrosion in an aerated aqueous solution.[69,70]

Similar studies based on the X-ray photoelectron spectroscopic (XPS) investigations showed that the corrosion prevention of an aluminum alloy by vanadate is achieved *via* a complex series of redox reactions on the cathodic IMPs sites.[68,71] In vanadate treatments, many forms of vanadium ions can be introduced, referring to an anionic coordination complex of vanadium (usually oxoanions) that mostly exists in one of the high oxidation states +3, +4, or +5.[72] These vanadate species are usually unstable and quickly hydrolyzed in aerated aqueous solutions. For example, in anticorrosion treatments, the V^{5+} species would be reduced to V^{4+} and/or V^{3+} on the cathodic site followed by subsequent oxidation, forming a vanadium-rich film, where the V^{4+} and/or V^{5+} oxidation states abundantly exist.[68,71] This film would develop over a prolonged immersion time, whereby its thickness increases with the immersion time and temperature.

Based on these results, it can be postulated that in our case, oxygen is first reduced according to the above eqn (2) and (3). On the other side, the MOF crystals within the epoxy matrix slowly dissociate, releasing V^{3+} ions, which are then dissolved into the solution.[52] Generally, the V^{3+} ions are readily oxidized in the air or aerated solutions.[73] These ions would be reacting with the oxidizing species at the cathodic sites forming V^{4+} and/or V^{5+} as follows:

$$2V^{3+} + 3/2H_2O_2 \rightarrow V^{4+} + V^{5+} + 3OH^- \quad (8)$$

Finally, the produced V^{4+}/V^{5+} ions would precipitate on the IMPs forming a stable film that goes against any further oxygen reduction, consequently reducing the corrosion rate of AA2024 in aerated NaCl solution.[49] The development of this vanadate

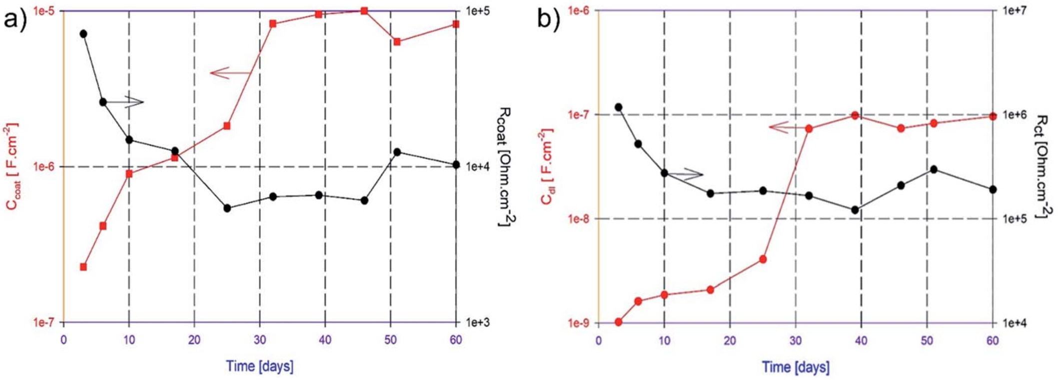

Fig. 13 The change in (a) C_{coat} and R_{coat} and (b) C_{dl} and R_{ct} values regarding the MOF/epoxy coated AA2024 sample in 3.5% NaCl solution *versus* the immersion time.

film proceeds during the first three weeks of immersion, explaining the initial decrease in the impedance of the MOF/epoxy coating reported above (Fig. 9a).

The strategy of applying corrosion inhibitors in this type of alloys is to reduce the inhomogeneity of the surface potential, hence decreasing the galvanic corrosion. The addition of any inhibitor needs to be controlled and targeted towards specific areas.[74] Thus, the presence of the V-MOF (MIL-47as) crystals not only controls the leaching of vanadium within the matrix but also influences homogeneity among the layers. These MOF crystals interact with the aqueous solution molecules along with their accompanying oxidizing species that slowly diffuse from the medium to the metal surface through the MOF/epoxy matrix. The MIL-47as particles are slightly soluble in similar aqueous media, governing the leaching of the vanadate ions from MOF structure into the epoxy matrix and targeting the surface areas where the corrosive solution would diffuse.[52] The released V^{3+} ions would directly move and precipitate at these cathodic sites, IMPs, to decrease oxygen reduction reaction.

Conclusions

In summary, the vanadium MIL-47 metal–organic framework was successfully synthesized *via* a solvothermal method. Such a synthesis combines several advantages: (a) the reaction does not require the addition of modulators/mineralizers like monocarboxylic acids, which makes it a simple, direct, and straightforward route. (b) The reaction occurs at a lower reaction temperature and duration than other studies reported before (180 °C/20 h instead of 220 °C/72 h). (c) Vanadium pentoxide (V_2O_5) was employed as a suitable metal precursor; it is inexpensive and highly available. Moreover, the characterization of the products showed that the achieved MOF was pure without any metal-oxide contamination. In addition, the as-synthesized MOF had the same thermal stability compared to those obtained *via* other synthesis techniques. The prepared MOF was then added to epoxy to produce an advanced coating that applies to aluminum alloy AA2024 for corrosion protection in a harsh chloride-rich environment. Investigation *via* SEM-EDX for the MOF/epoxy coating revealed a uniform coating with a constant thickness of 10 ± 2 μm and a homogeneous distribution of the MOF crystals within the thermoset epoxy matrix. Compared to the neat-epoxy coating, the inclusion of small loading of the MOF particles (10 wt%) increases the hydrophilicity of the coating. However, they can extend the lifetime protection of the metal surface 3 folds. According to the results of the EIS experiments, the MOF/epoxy coating would have the same behavior as the neat epoxy one for the first three weeks, whereby the corrosive species diffuse into the coating. Nevertheless, the MIL-47as crystals would then interact with these diffusing molecules releasing vanadate ions and developing a protective film at the intermetallic particles. Such a protective film provides extended cathodic protection.

Conflicts of interest

There are no conflicts to declare.

Acknowledgements

We are thankful to the Arab Republic of Egypt – Ministry of Defense, for providing financial support to M. Y. Zorainy. The authors are also grateful to the Natural Sciences and Engineering Research Council of Canada (NSERC) for its support, as well as to the Fonds de Recherche du Québec – Nature et Technologies (FRQNT). This research was undertaken, in part, thanks to funding from the Canada Research Chair program.

References

1 C. Xu, R. Fang, R. Luque, L. Chen and Y. Li, Functional metal–organic frameworks for catalytic applications, *Coord. Chem. Rev.*, 2019, **388**, 268–292, DOI: 10.1016/j.ccr.2019.03.005.

2 C. Petit, Present and future of MOF research in the field of adsorption and molecular separation, *Curr. Opin. Chem. Eng.*, 2018, **20**, 132–142, DOI: 10.1016/j.coche.2018.04.004.

3 J. Caro, Quo Vadis, MOF?, *Chem. Ing. Tech.*, 2018, **90**(11), 1759–1768, DOI: 10.1002/cite.201800034.

4 P. Kumar, A. Deep and K.-H. Kim, Metal organic frameworks for sensing applications, *Trac. Trends Anal. Chem.*, 2015, **73**, 39–53, DOI: 10.1016/j.trac.2015.04.009.

5 C.-Y. Sun, C. Qin, X.-L. Wang and Z.-M. Su, Metal-organic frameworks as potential drug delivery systems, *Expert Opin. Drug Deliv.*, 2013, **10**(1), 89–101, DOI: 10.1517/17425247.2013.741583.

6 O. M. Yaghi, M. J. Kalmutzki, and C. S. Diercks, *Introduction to Reticular Chemistry: Metal-Organic Frameworks and Covalent Organic Frameworks*, John Wiley & Sons. Weinheim, Germany, 2019.

7 N. Stock and S. Biswas, Synthesis of Metal-Organic Frameworks (MOFs): Routes to Various MOF Topologies, Morphologies, and Composites, *Chem. Rev.*, 2012, **112**(2), 933–969, DOI: 10.1021/cr200304e.

8 P. Van Der Voort, K. Leus, Y.-Y. Liu, M. Vandichel, V. Van Speybroeck, M. Waroquier and S. Biswas, Vanadium metal–organic frameworks: structures and applications, *New J. Chem.*, 2014, **38**(5), 1853–1867, DOI: 10.1039/C3NJ01130E.

9 K. Barthelet, J. Marrot, D. Riou and G. Férey, A Breathing Hybrid Organic–Inorganic Solid with Very Large Pores and High Magnetic Characteristics, *Angew. Chem., Int. Ed.*, 2002, **41**(2), 281–284, DOI: 10.1002/1521-3773(20020118)41:2<281::AID-ANIE281>3.0.CO;2-Y.

10 M. Y. Zorainy, M. Gar Alalm, S. Kaliaguine and D. C. Boffito, Revisiting the MIL-101 Metal-Organic Framework: Design, Synthesis, Modifications, Advances, and Recent Applications, *J. Mater. Chem. A*, 2021, **9**(39), 22159–22217, DOI: 10.1039/D1TA06238G.

11 A. Schneemann, V. Bon, I. Schwedler, I. Senkovska, S. Kaskel and R. A. Fischer, Flexible metal–organic frameworks, *Chem. Soc. Rev.*, 2014, **43**(16), 6062–6096, DOI: 10.1039/C4CS00101J.

12 C. Serre, F. Millange, C. Thouvenot, M. Noguès, G. Marsolier, D. Louër and G. Férey, Very Large Breathing Effect in the

First Nanoporous Chromium(III)-Based Solids: MIL-53 or CrIII(OH)·{O2C−C6H4−CO2}·{HO2C−C6H4−CO2H} x·H2Oy, *J. Am. Chem. Soc.*, 2002, **124**(45), 13519–13526, DOI: 10.1021/ja0276974.

13 J. P. S. Mowat, S. R. Miller, A. M. Z. Slawin, V. R. Seymour, S. E. Ashbrook and P. A. Wright, Synthesis, characterisation and adsorption properties of microporous scandium carboxylates with rigid and flexible frameworks, *Microporous Mesoporous Mater.*, 2011, **142**(1), 322–333, DOI: 10.1016/j.micromeso.2010.12.016.

14 F. Millange, N. Guillou, R. I. Walton, J.-M. Grenèche, I. Margiolaki and G. Férey, Effect of the nature of the metal on the breathing steps in MOFs with dynamic frameworks, *Chem. Commun.*, 2008, **39**, 4732–4734, DOI: 10.1039/B809419E.

15 T. Loiseau, C. Serre, C. Huguenard, G. Fink, F. Taulelle, M. Henry, T. Bataille and G. Férey, A Rationale for the Large Breathing of the Porous Aluminum Terephthalate (MIL-53) Upon Hydration, *Chem. - Eur J.*, 2004, **10**(6), 1373–1382, DOI: 10.1002/chem.200305413.

16 C. Volkringer, T. Loiseau, N. Guillou, G. Férey, E. Elkaïm and A. Vimont, XRD and IR structural investigations of a particular breathing effect in the MOF-type gallium terephthalate MIL-53(Ga), *Dalton Trans.*, 2009, **12**, 2241–2249, DOI: 10.1039/B817563B.

17 E. V. Anokhina, M. Vougo-Zanda, X. Wang and A. J. Jacobson, In(OH)BDC·0.75BDCH2 (BDC = Benzenedicarboxylate), a Hybrid Inorganic−Organic Vernier Structure, *J. Am. Chem. Soc.*, 2005, **127**(43), 15000–15001, DOI: 10.1021/ja055757a.

18 M. Hosseini, D. E. P. Vanpoucke, P. Giannozzi, M. Berahman and N. Hadipour, Investigation of structural, electronic and magnetic properties of breathing metal–organic framework MIL-47(Mn): a first principles approach, *RSC Adv.*, 2020, **10**(8), 4786–4794, DOI: 10.1039/C9RA09196C.

19 Y.-X. Tan, Y.-P. He, Y. Zhang, Y.-J. Zheng and J. Zhang, Solvent controlled assembly of four Mn(ii)-2,5-thiophenedicarboxylate frameworks with rod-packing architectures and magnetic properties, *CrystEngComm*, 2013, **15**(30), 6009–6014, DOI: 10.1039/C3CE40677F.

20 G. Zhan and H. C. Zeng, Alternative synthetic approaches for metal–organic frameworks: transformation from solid matters, *Chem. Commun.*, 2017, **53**(1), 72–81, DOI: 10.1039/C6CC07094A.

21 J. Reboul, S. Furukawa, N. Horike, M. Tsotsalas, K. Hirai, H. Uehara, M. Kondo, N. Louvain, O. Sakata and S. Kitagawa, Mesoscopic architectures of porous coordination polymers fabricated by pseudomorphic replication, *Nat. Mater.*, 2012, **11**(8), 717–723, DOI: 10.1038/nmat3359.

22 S. Biswas, D. E. P. Vanpoucke, T. Verstraelen, M. Vandichel, S. Couck, K. Leus, Y.-Y. Liu, M. Waroquier, V. Van Speybroeck, J. F. M. Denayer and P. Van Der Voort, New Functionalized Metal–Organic Frameworks MIL-47-X (X = −Cl, −Br, −CH3, −CF3, −OH, −OCH3): Synthesis, Characterization, and CO2 Adsorption Properties, *J. Phys. Chem. C*, 2013, **117**(44), 22784–22796, DOI: 10.1021/jp406835n.

23 H. Leclerc, T. Devic, S. Devautour-Vinot, P. Bazin, N. Audebrand, G. Férey, M. Daturi, A. Vimont and G. Clet, Influence of the Oxidation State of the Metal Center on the Flexibility and Adsorption Properties of a Porous Metal Organic Framework: MIL-47(V), *J. Phys. Chem. C*, 2011, **115**(40), 19828–19840, DOI: 10.1021/jp206655y.

24 N. A. Khan, J. W. Jun, J. H. Jeong and S. H. Jhung, Remarkable adsorptive performance of a metal–organic framework, vanadium-benzenedicarboxylate (MIL-47), for benzothiophene, *Chem. Commun.*, 2011, **47**(4), 1306–1308, DOI: 10.1039/C0CC04759G.

25 P. G. Yot, Q. Ma, J. Haines, Q. Yang, A. Ghoufi, T. Devic, C. Serre, V. Dmitriev, G. Férey, C. Zhong and G. Maurin, Large breathing of the MOF MIL-47(VIV) under mechanical pressure: a joint experimental–modelling exploration, *Chem. Sci.*, 2012, **3**(4), 1100–1104, DOI: 10.1039/C2SC00745B.

26 X. Wang, J. Eckert, L. Liu and A. J. Jacobson, Breathing and Twisting: An Investigation of Framework Deformation and Guest Packing in Single Crystals of a Microporous Vanadium Benzenedicarboxylate, *Inorg. Chem.*, 2011, **50**(5), 2028–2036, DOI: 10.1021/ic1025087.

27 L. Alaerts, C. E. A. Kirschhock, M. Maes, M. A. van der Veen, V. Finsy, A. Depla, J. A. Martens, G. V. Baron, P. A. Jacobs, J. F. M. Denayer and D. E. De Vos, Selective Adsorption and Separation of Xylene Isomers and Ethylbenzene with the Microporous Vanadium(IV) Terephthalate MIL-47, *Angew. Chem., Int. Ed.*, 2007, **46**(23), 4293–4297, DOI: 10.1002/anie.200700056.

28 K. Leus, M. Vandichel, Y.-Y. Liu, I. Muylaert, J. Musschoot, S. Pyl, H. Vrielinck, F. Callens, G. B. Marin, C. Detavernier, P. V. Wiper, Y. Z. Khimyak, M. Waroquier, V. Van Speybroeck and P. Van Der Voort, The coordinatively saturated vanadium MIL-47 as a low leaching heterogeneous catalyst in the oxidation of cyclohexene, *J. Catal.*, 2012, **285**(1), 196–207, DOI: 10.1016/j.jcat.2011.09.014.

29 B. Niu, B. Yao, M. Zhu, H. Guo, S. Ying and Z. Chen, Carbon paste electrode modified with fern leave-like MIL-47(as) for electrochemical simultaneous detection of Pb(II), Cu(II) and Hg(II), *J. Electroanal. Chem.*, 2021, **886**, 115121, DOI: 10.1016/j.jelechem.2021.115121.

30 X. Wang, L. Liu and A. J. Jacobson, Intercalation of Organic Molecules into Vanadium(IV) Benzenedicarboxylate: Adsorbate Structure and Selective Absorption of Organosulfur Compounds, *Angew. Chem., Int. Ed.*, 2006, **45**(39), 6499–6503, DOI: 10.1002/anie.200602556.

31 W. Kaveevivitchai, X. Wang, L. Liu and A. J. Jacobson, Two Distinct Redox Intercalation Reactions of Hydroquinone with Porous Vanadium Benzenedicarboxylate MIL-47, *Inorg. Chem.*, 2015, **54**(4), 1822–1828, DOI: 10.1021/ic502730y.

32 J. Reboul, K. Yoshida, S. Furukawa and S. Kitagawa, Reductive coordination replication of V2O5 sacrificial macrostructures into vanadium-based porous coordination

polymers, *CrystEngComm*, 2015, **17**(2), 323–330, DOI: 10.1039/C4CE01501K.

33 C. Vargel, *Corrosion of aluminium*, 2nd edn, Elsevier, 2020.

34 J. K. Wessel, *The handbook of advanced materials: enabling new designs*, John Wiley & Sons, New Jersey, USA, 1st edn, 2004.

35 C. Verma, L. O. Olasunkanmi, E. D. Akpan, M. A. Quraishi, O. Dagdag, M. El Gouri, E.-S. M. Sherif and E. E. Ebenso, Epoxy resins as anticorrosive polymeric materials: A review, *React. Funct. Polym.*, 2020, **156**, 104741, DOI: 10.1016/j.reactfunctpolym.2020.104741.

36 F. Seidi, M. Jouyandeh, M. Taghizadeh, A. Taghizadeh, H. Vahabi, S. Habibzadeh, K. Formela and M. R. Saeb, Metal-Organic Framework (MOF)/Epoxy Coatings: A Review, *Materials*, 2020, **13**(12), 2881, DOI: 10.3390/ma13122881.

37 M. Zhang, L. Ma, L. Wang, Y. Sun and Y. Liu, Insights into the Use of Metal–Organic Framework As High-Performance Anticorrosion Coatings, *ACS Appl. Mater. Interfaces*, 2018, **10**(3), 2259–2263, DOI: 10.1021/acsami.7b18713.

38 Y. J. Tarzanagh, D. Seifzadeh, Z. Rajabalizadeh, A. Habibi-Yangjeh, A. Khodayari and S. Sohrabnezhad, Sol-gel/MOF nanocomposite for effective protection of 2024 aluminum alloy against corrosion, *Surf. Coat. Technol.*, 2019, **380**, 125038, DOI: 10.1016/j.surfcoat.2019.125038.

39 S. Duan, B. Dou, X. Lin, S. Zhao, W. Emori, J. Pan, H. Hu and H. Xiao, Influence of active nanofiller ZIF-8 metal-organic framework (MOF) by microemulsion method on anticorrosion of epoxy coatings, *Colloids Surf., A*, 2021, **624**, 126836, DOI: 10.1016/j.colsurfa.2021.126836.

40 N. Keshmiri, P. Najmi, M. Ramezanzadeh and B. Ramezanzadeh, Designing an eco-friendly lanthanide-based metal organic framework (MOF) assembled graphene-oxide with superior active anti-corrosion performance in epoxy composite, *J. Clean. Prod.*, 2021, **319**, 128732, DOI: 10.1016/j.jclepro.2021.128732.

41 S. M. Lashgari, H. Yari, M. Mahdavian, B. Ramezanzadeh, G. Bahlakeh and M. Ramezanzadeh, Application of nanoporous cobalt-based ZIF-67 metal-organic framework (MOF) for construction of an epoxy-composite coating with superior anti-corrosion properties, *Corros. Sci.*, 2021, **178**, 109099, DOI: 10.1016/j.corsci.2020.109099.

42 S. M. Lashgari, H. Yari, M. Mahdavian, B. Ramezanzadeh, G. Bahlakeh and M. Ramezanzadeh, Synthesis of graphene oxide nanosheets decorated by nanoporous zeolite-imidazole (ZIF-67) based metal-organic framework with controlled-release corrosion inhibitor performance: Experimental and detailed DFT-D theoretical explorations, *J. Hazard. Mater.*, 2021, **404**, 124068, DOI: 10.1016/j.jhazmat.2020.124068.

43 M. Ramezanzadeh, B. Ramezanzadeh, G. Bahlakeh, A. Tati and M. Mahdavian, Development of an active/barrier bi-functional anti-corrosion system based on the epoxy nanocomposite loaded with highly-coordinated functionalized zirconium-based nanoporous metal-organic framework (Zr-MOF), *Chem. Eng. J.*, 2021, **408**, 127361, DOI: 10.1016/j.cej.2020.127361.

44 M. Ramezanzadeh, B. Ramezanzadeh, M. Mahdavian and G. Bahlakeh, Development of metal-organic framework (MOF) decorated graphene oxide nanoplatforms for anti-corrosion epoxy coatings, *Carbon*, 2020, **161**, 231–251, DOI: 10.1016/j.carbon.2020.01.082.

45 N. Wang, Y. Zhang, J. Chen, J. Zhang and Q. Fang, Dopamine modified metal-organic frameworks on anti-corrosion properties of waterborne epoxy coatings, *Prog. Org. Coat.*, 2017, **109**, 126–134, DOI: 10.1016/j.porgcoat.2017.04.024.

46 A. Morozan and F. Jaouen, Metal organic frameworks for electrochemical applications, *Energy Environ. Sci.*, 2012, **5**(11), 9269–9290, DOI: 10.1039/C2EE22989G.

47 M. Jouyandeh, F. Tikhani, M. Shabanian, F. Movahedi, S. Moghari, V. Akbari, X. Gabrion, P. Laheurte, H. Vahabi and M. R. Saeb, Synthesis, characterization, and high potential of 3D metal–organic framework (MOF) nanoparticles for curing with epoxy, *J. Alloys Compd.*, 2020, **829**, 154547, DOI: 10.1016/j.jallcom.2020.154547.

48 M. Zorainy, D. C. Boffito, M. Gobara, A. Baraka, I. Naeem and H. Tantawy, Synthesis of a novel Ce(iii)/melamine coordination polymer and its application for corrosion protection of AA2024 in NaCl solution, *RSC Adv.*, 2021, **11**(11), 6330–6345, DOI: 10.1039/D0RA08587A.

49 M. Gobara, A. Baraka, R. Akid and M. Zorainy, Corrosion protection mechanism of Ce4+/organic inhibitor for AA2024 in 3.5% NaCl, *RSC Adv.*, 2020, **10**(4), 2227–2240, DOI: 10.1039/C9RA09552G.

50 F. Millange, C. Serre and G. Férey, Synthesis, structure determination and properties of MIL-53as and MIL-53ht: the first Criii hybrid inorganic–organic microporous solids: Criii(OH)·{O2C–C6H4–CO2}·{HO2C–C6H4–CO2H}x, *Chem. Commun.*, 2002, **8**, 822–823, DOI: 10.1039/B201381A.

51 J. A. A. Ketelaar, Crystal Structure and Shape of Colloidal Particles of Vanadium Pentoxide, *Nature*, 1936, **137**(3460), 316, DOI: 10.1038/137316a0.

52 I. J. Kang, N. A. Khan, E. Haque and S. H. Jhung, Chemical and Thermal Stability of Isotypic Metal–Organic Frameworks: Effect of Metal Ions, *Chem. - Eur J.*, 2011, **17**(23), 6437–6442, DOI: 10.1002/chem.201100316.

53 M. Gobara, H. Kamel, R. Akid and A. Baraka, Corrosion behaviour of AA2024 coated with an acid-soluble collagen/hybrid silica sol–gel matrix, *Prog. Org. Coat.*, 2015, **89**, 57–66, DOI: 10.1016/j.porgcoat.2015.07.026.

54 A. S. Hamdy, I. Doench and H. Möhwald, Intelligent self-healing corrosion resistant vanadia coating for AA2024, *Thin Solid Films*, 2011, **520**(5), 1668–1678, DOI: 10.1016/j.tsf.2011.05.080.

55 G. S. Chen, M. Gao and R. P. Wei, Microconstituent-Induced Pitting Corrosion in Aluminum Alloy 2024-T3, *Corrosion*, 1996, **52**(1), 8–15, DOI: 10.5006/1.3292099.

56 D. Ho, N. Brack, J. Scully, T. Markley, M. Forsyth and B. Hinton, Cerium dibutylphosphate as a corrosion inhibitor for AA2024-T3 aluminum alloys, *J. Electrochem. Soc.*, 2006, **153**(9), B392, DOI: 10.1149/1.2217260.

57 R. Akid, M. Gobara and H. Wang, Corrosion protection performance of novel hybrid polyaniline/sol–gel coatings on an aluminium 2024 alloy in neutral, alkaline and acidic

solutions, *Electrochim. Acta*, 2011, **56**(5), 2483–2492, DOI: 10.1016/j.electacta.2010.12.032.

58 B. D. Chambers and S. R. Taylor, The high throughput assessment of aluminium alloy corrosion using fluorometric methods. Part II – A combinatorial study of corrosion inhibitors and synergistic combinations, *Corros. Sci.*, 2007, **49**(3), 1597–1609, DOI: 10.1016/j.corsci.2006.08.006.

59 O. A. Lopez-Garrity, Corrosion inhibition mechanisms of aluminum alloy 2024-T3 by selected non-chromate inhibitors, PhD thesis, The Ohio State University, Ann Arbor, 3670758, 2013, Available: https://www.proquest.com/dissertations-theses/corrosion-inhibition-mechanisms-aluminum-alloy/docview/1647138206/se-2?accountid=40695.

60 R. G. Buchheit, R. P. Grant, P. F. Hlava, B. McKenzie and G. L. Zender, Local Dissolution Phenomena Associated with S Phase (Al2CuMg) Particles in Aluminum Alloy 2024-T3, *J. Electrochem. Soc.*, 1997, **144**(8), 2621–2628, DOI: 10.1149/1.1837874.

61 K. A. Yasakau, M. L. Zheludkevich, S. V. Lamaka and M. G. S. Ferreira, Mechanism of Corrosion Inhibition of AA2024 by Rare-Earth Compounds, *J. Phys. Chem. B*, 2006, **110**(11), 5515–5528, DOI: 10.1021/jp0560664.

62 F. Salles, S. Bourrelly, H. Jobic, T. Devic, V. Guillerm, P. Llewellyn, C. Serre, G. Ferey and G. Maurin, Molecular Insight into the Adsorption and Diffusion of Water in the Versatile Hydrophilic/Hydrophobic Flexible MIL-53(Cr) MOF, *J. Phys. Chem. C*, 2011, **115**(21), 10764–10776, DOI: 10.1021/jp202147m.

63 M. A. Amin and M. M. Ibrahim, Corrosion and corrosion control of mild steel in concentrated H2SO4 solutions by a newly synthesized glycine derivative, *Corros. Sci.*, 2011, **53**(3), 873–885, DOI: 10.1016/j.corsci.2010.10.022.

64 R. Jindal, V. S. Raja, M. A. Gibson, M. J. Styles, T. J. Bastow and C. R. Hutchinson, Effect of annealing below the crystallization temperature on the corrosion behavior of Al–Ni–Y metallic glasses, *Corros. Sci.*, 2014, **84**, 54–65, DOI: 10.1016/j.corsci.2014.03.015.

65 C. Fan, Y. Liu, X. Yin, J. Shi and K. Dilger, Electrochemical Behavior and Interfacial Delamination of a Polymer-Coated Galvanized Steel System in Acid Media, *ACS Omega*, 2021, **6**(31), 20331–20340, DOI: 10.1021/acsomega.1c02270.

66 W. Zhang, Y.-C. Wu and H.-J. Li, Apostichopus japonicus polysaccharide as efficient sustainable inhibitor for mild steel against hydrochloric acid corrosion, *J. Mol. Liq.*, 2021, **321**, 114923, DOI: 10.1016/j.molliq.2020.114923.

67 K. D. Ralston, S. Chrisanti, T. L. Young and R. G. Buchheit, Corrosion inhibition of aluminum alloy 2024-T3 by aqueous vanadium species, *J. Electrochem. Soc.*, 2008, **155**(7), C350.

68 M. Iannuzzi and G. S. Frankel, Mechanisms of corrosion inhibition of AA2024-T3 by vanadates, *Corros. Sci.*, 2007, **49**(5), 2371–2391, DOI: 10.1016/j.corsci.2006.10.027.

69 T. Zheng, J. Liu, L. Wang, J. Wang and G. Jia, Corrosion inhibition of AA2024-T3 in alkaline solution by disodium-N-dodecyliminodiacetate: Experimental and theoretical studies, *Colloids Surf., A*, 2021, **626**, 126989, DOI: 10.1016/j.colsurfa.2021.126989.

70 C. Li, X. Guo and G. S. Frankel, Corrosion inhibition of AA2024-T3 by a coating containing dual-pH sensitive, corrosion inhibitor loaded microspheres, *Corros. Sci.*, 2021, **192**, 109835, DOI: 10.1016/j.corsci.2021.109835.

71 D. S. Kharitonov, J. Sommertune, C. Örnek, J. Ryl, I. I. Kurilo, P. M. Claesson and J. Pan, Corrosion inhibition of aluminium alloy AA6063-T5 by vanadates: Local surface chemical events elucidated by confocal Raman micro-spectroscopy, *Corros. Sci.*, 2019, **148**, 237–250, DOI: 10.1016/j.corsci.2018.12.011.

72 B. Yang, J. He, G. Zhang, and J. Guo, *Vanadium: Extraction, Manufacturing and Applications*, Elsevier, 1st edn, 2021.

73 D. C. Crans and A. S. Tracey, The Chemistry of Vanadium in Aqueous and Nonaqueous Solution, in *Vanadium Compounds, ACS Symposium Series, no. 711*, American Chemical Society, 1998, vol. 711, ch. 1, pp. 2–29.

74 A. C. Bouali, N. M. André, M. R. Silva Campos, M. Serdechnova, J. F. dos Santos, S. T. Amancio-Filho and M. L. Zheludkevich, Influence of LDH conversion coatings on the adhesion and corrosion protection of friction spot-joined AA2024-T3/CF-PPS, *J. Mater. Sci. Technol.*, 2021, **67**, 197–210, DOI: 10.1016/j.jmst.2020.06.038.